Journal of Volcanology and Geothermal Research 434 (2023) 107745

Contents lists available at ScienceDirect

Journal of Volcanology and Geothermal Research

journal homepage: www.journals.elsevier.com/journal-of-volcanology-and-geothermal-research

The tsunamigenic potential of landslide-generated tsunamis on the Vavilov seamount

G. Gallotti [a,*], F. Zaniboni [a], D. Arcangeli [b], C. Angeli [a], A. Armigliato [a], L. Cocchi [c], F. Muccini [c], M. Zanetti [a], S. Tinti [a], G. Ventura [c,d]

[a] University of Bologna, Department of Physics and Astronomy "Augusto Righi" (DIFA), Bologna, Italy
[b] Formerly at Istituto Nazionale di Geofisica e Vulcanologia (INGV), Bologna, Italy
[c] Istituto Nazionale di Geofisica e Vulcanologia (INGV), Roma, Italy
[d] Istituto per lo Studio degli impatti Antropici e Sostenibilità in ambiente marino, Consiglio Nazionale delle Ricerche, Capo Granitola, TP, Italy

ARTICLE INFO

Keywords:
Tsunami
Submarine landslide
Submarine volcano
Tyrrhenian Sea

ABSTRACT

The investigation of submarine volcanoes and the tsunamigenic potential of possible movements on their flanks is arduous. In most cases, the lack of specific information about the eruptions' history and their consequences does not allow a comprehensive analysis in terms of hazard. Nevertheless, useful clues on the possible occurrence of mass movements on seamounts can be obtained from a series of research fields. These account for morphological studies, observations of hydrothermal activity, collection of geophysical data (for example, detailed DEM, seismic profiles, magnetic data), etc. In this context, this study presents new bathymetric data of the Vavilov submarine volcano (Tyrrhenian Sea, Italy) and a detailed morphological analysis of the structure. The latter allows the identification of zones potentially prone to mass movements and the development of numerical scenarios to investigate the tsunami potential associated to these movements on the Vavilov flanks. Results prove that the waves generated by the mass displacements in the proposed scenarios (involving sliding volumes between 0.32 km^3 and 1.7 km^3) reach maximum values in the order of centimetres, not considering dispersive effects. Eventually, a scenario involving the partial collapse of the west flank of the Vavilov Seamount is simulated, although the occurrence of such an event in the past is still debated due to the uncertainties related to the origin and development of the volcano dome. In this scenario, water elevation as high as 10 m are found in large portions of the Tyrrhenian coasts: waves are large enough to emplace sizeable tsunami deposits onshore, that could have been preserved until today in some specific stretches of the coast and could be detected by a finalised geological search. This study belongs to a series of works devoted to the submarine structures of the Tyrrhenian Sea aiming to disclose the tsunamigenic potential of submarine mass movements on their flanks.

1. Introduction

The recent lateral collapse of the Anak Krakatau volcano and the presumed caldera collapse of the Hunga Tonga- Hunga Haʻapai volcano have boosted the attention of the research community to the local investigation and understanding of landslide-induced tsunamis in volcanic environments (Grilli et al., 2019; Williams et al., 2019; Paris et al., 2020; Ren et al., 2020). In the numerical investigation of these events, several aspects must be considered, ranging from the source mechanism (e.g., Nagai et al., 2021) to the wave propagation in the basin surrounding the source area (e.g., Dao and Tkalich, 2007). To this goal, a series of techniques have been proposed in the literature with satisfying results (for recent reviews, see e.g., Yavari-Ramshe and Ataie-Ashtiani, 2016, and Kirby et al., 2022). The application of these methods to real cases requires an a priori fundamental step: a deep and detailed description of the landslide location (e.g., volcanic islands, seamounts, submarine volcanoes). In this study, we focus our attention on the Vavilov submarine volcano, located in the central part of the Tyrrhenian basin, Italy. In the past years, a series of works have been devoted to the investigation of the numerous submarine structures of the Tyrrhenian Sea (Rovere et al., 2016; Cocchi et al., 2017) also in a landslide-generated tsunami perspective (Fornaciai et al., 2019; Esposti Ongaro et al., 2021; Gallotti et al., 2020; Gallotti et al., 2021). This latter aspect is an arduous task on this kind of remote and poorly investigated

* Corresponding author.
E-mail address: glauco.gallotti2@unibo.it (G. Gallotti).

https://doi.org/10.1016/j.jvolgeores.2023.107745
Received 3 May 2022; Received in revised form 28 December 2022; Accepted 4 January 2023
Available online 6 January 2023

structures due to the lack of specific information about the volcano and its characteristics. Specifically, two classes of information are needed to build a tsunami hazard evaluation related to landslide-triggered tsunamis. First, detailed geophysical data accounting for the morphology and structure of the relief potentially affected by gravity instability and landslides; secondly, the seismological and volcanological history of the area to estimate recurrence times for the specific event and to perform probabilistic analyses. The latter aspects are lacking in the case of the Tyrrhenian seamounts. Thus, the only possible realistic approach to this problem is the construction of scenarios based on the available geophysical data and on geomorphological considerations. This procedure, though incomplete, allows a first important step in the evaluation of the potentially more dangerous structures.

The Tyrrhenian Sea is a back-arc basin consisting of three oceanic sub-basins, i.e. the Marsili, Magnaghi, and Vavilov basins. They represent back-arc extensional structures associated with the north-westward subduction of the Ionian Sea and Adriatic plate below the Calabrian Arc and Apennine chain, respectively (Malinverno and Ryan, 1986; Faccenna et al., 2001). The Tyrrhenian Sea includes 33 registered volcanic seamounts (Pensa et al., 2019) and the 2800 m high Vavilov seamount is among the largest ones measuring about 30 km in length and 14 km in width. Because of N10°E elongation and occurrence of scars and morphological wedges, the Vavilov seamount could represent, along with other seamounts of the Tyrrhenian Sea as the Marsili and Palinuro seamounts, a source of potential tsunami hazard especially for the western coasts of mainland Italy. Here, we present new bathymetric data and analyze the morphology of Vavilov by identifying potentially unstable flanks. We perform tsunami simulations on the selected different unstable flanks. Our study mainly concentrates on the simulation of potential mass movements and their effects in terms of generated tsunami on the coasts of Italy bounding the Tyrrhenian Sea. In addition, we perform a simulation of a potential past collapse that could have affected the Vavilov western flank. Our results shed new light on the morphology and structure of the Vavilov Seamount and have implications for the evaluation of tsunami hazard from seafloor sliding processes affecting volcanic seamounts.

2. Geological setting

The geodynamic evolution of the central Mediterranean Sea is the result of the collision between African and Eurasian plates. Since the Oligocene, the tectonic evolution of this area was affected by sinking and retreating of the Ionian subducting slab inducing an eastward migration of the entire Apennine-Maghrebide system (Malinverno and Ryan, 1986; Kastens et al., 1988; Doglioni, 1991; Doglioni et al., 1999, 2004). The eastward migration of the subduction system acted as stretching of the continental crust and evolving in steps with back-arc formation occurring first in the Provencal area, then in the Valencia domain and finally in the Tyrrhenian Sea. Since the Tortonian, the roll back process occurred in the north Tyrrhenian Sea with a main *E*-W direction, triggering a slow extension rate (1–2 cm/y) and the formation of a set of N-S and NE-SW oriented basins associated to magmatic intrusions and minor alkaline volcanism (Fig. 1; Faccenna et al., 1997; Mauffret et al., 1999). During the Pliocene, the eastward migration of the subduction system evolved with an increasing of the deformation rate with a crustal thinning and emplacement of spots of oceanic crust

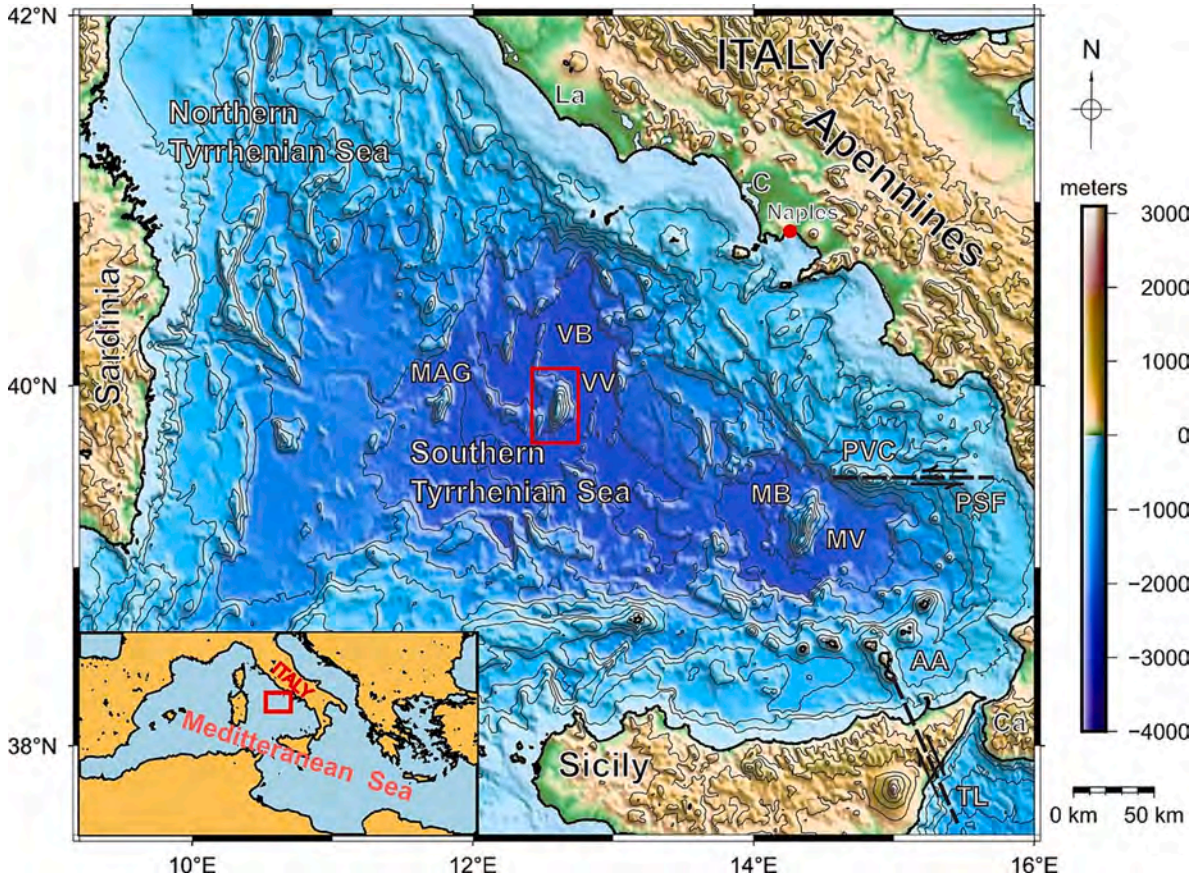

Fig. 1. Bathymetry map of the Tyrrhenian Sea (data from GEBCO - 15 arc *sec* resolution, from Tozer et al., 2019) showing major tectonic and volcanic features: Magnaghi Volcano (MAG); Vavilov Basin (VB) and Vavilov Volcano (VV, marked with a red box); Marsili Basin (MB) and Marsili Volcano (MV); Aeolian Arc (AA); Palinuro Volcanic Complex (PVC); Latium region (La); Campanian region (C); Calabrian region (Ca). Tindari Letojanni Tear Fault (TL) and Palinuro Step Fault (PSF) are from De Astis et al. (2003) and Cocchi et al. (2017), respectively. (For interpretation of the references to colour in this figure legend, the reader is referred to the web version of this article.)

initially in Vavilov (5.5 Ma) and subsequently in the Marsili (2.0) back-arc basins (Fig. 1; Royden, 1988; Patacca et al., 1990; Kastens et al., 1988; Faccenna et al., 1997; Cocchi et al., 2009). Consequently, arc-related volcanism migrated in a southeast direction, from Sardinia to the current position of the Aeolian arc, forming the present-day arc and back-arc configuration of the southern Tyrrhenian area (Fig. 1).

The Vavilov volcano (VV) is a large seamount located 180 km SW of Vesuvius and 250 km E of the Sardinia coasts in the south-central Tyrrhenian Sea (Fig. 1). The VV is made up of tholeiitic to alkali basalts (Robin et al., 1987) dated at Late Pliocene age (Savelli, 2002; Kastens et al., 1988) and it is the biggest topographic structure of the homonymous basin (Vavilov basin, VB) (Fig. 2). Several studies suggest the presence of oceanic crust in the Vavilov and Marsili basins (Mascle and Rehault, 1990; Sartori et al., 2004; Cella et al., 2008; Scrocca et al., 2012). Otherwise, Manu-Marfo et al. (2019), based on a 3D shear-wave velocity model, support the hypothesis on an exhumed mantle, as previously proposed by Prada et al. (2016), who ascribed Vp/Vs and Poisson's ratio to serpentinised peridotite.

The overall morphology of the volcano is dominated by an evident asymmetry of the two flanks (Fig. 2; Marani and Gamberi, 2004): the eastern flank has irregular topography, while the western one is smoother and steeper. K—Ar dating of fragments of pillows showed Pleistocene ages of 0.37 and 0.09 Ma (Robin et al., 1987), according with magnetic pattern (Faggioni et al., 1995; Savelli and Ligi, 2017) showing positive anomaly of the shallower portion of the volcano related to the Brunhes geomagnetic chron (< 0.78 Ma, Cande and Kent, 1995).

The base of the VV is also asymmetrical in *E*-W direction since the western side of the basin is about 200 m shallower than the eastern side (Fig. 2; 3400 m to 3600 m). Moreover, in the north-western sector of the VB, N100°E aligned structures produce a narrow-crested, few-hundred-meter-high relief. The similarities between the VB and the younger Marsili basin (MB) are known and widely reported in the literature. On the basis of the few data from IODP wells, both basins are floored by oceanic crust (Kastens et al., 1988; Sartori et al., 2004) and characterized by deep, flat bottom and axial volcanoes (Savelli and Schrieder, 1991) although Prada et al. (2016) report that the floor of the Tyrrhenian Sea basins consist of serpentinised peridotite.

On the basis of the observations and sampling from submersible Cyana, Robin et al. (1987) recognized 3 volcanic units forming the eastern flank of VV: W-tilted pillow lava flows (beneath 1500 m deep), radial lava flows (from 1500 m to 1000 m deep), scoriaceous lava flows (from 1000 m deep to the summit). Robin et al. (1987) recognized two principal eruptive centres above the 1500 m of depth and minor centres toward north and south aligned along a crustal fracture. The same authors speculated about a possible tectonic subsidence of at least 500 m during the late Pleistocene, and that the summit cones could be formed in a subaerial environment, despite no evidence of erosion.

3. Data and methods

3.1. Bathymetry data acquisition and processing

High resolution swath bathymetry acquisition of Vavilov seamount was achieved during oceanographic cruise VAV11 onboard the R/V Magnaghi of the Italian Navy in summer 2011. A Sea Beam 1050 multibeam system operating at 70 kHz frequency, featured by 126 beams and resolution of 1.5°, with a total swath aperture of 153°, was used to acquire the full coverage of the VV and part of the surrounding flat basin. The multibeam survey covered an overall area of >1800 km^2. Geo-referencing of multibeam data was ensured by using the differential GPS GNSS Trimble Pathfinder XRS-PRO; sound velocity profile casts were collected twice per day in order to evaluate variations of the sound velocity throughout the water column.

Raw bathymetric data was then processed using Caris Hips and Sips 8.1 computing an interpolated surface having a cell size resolution of 25

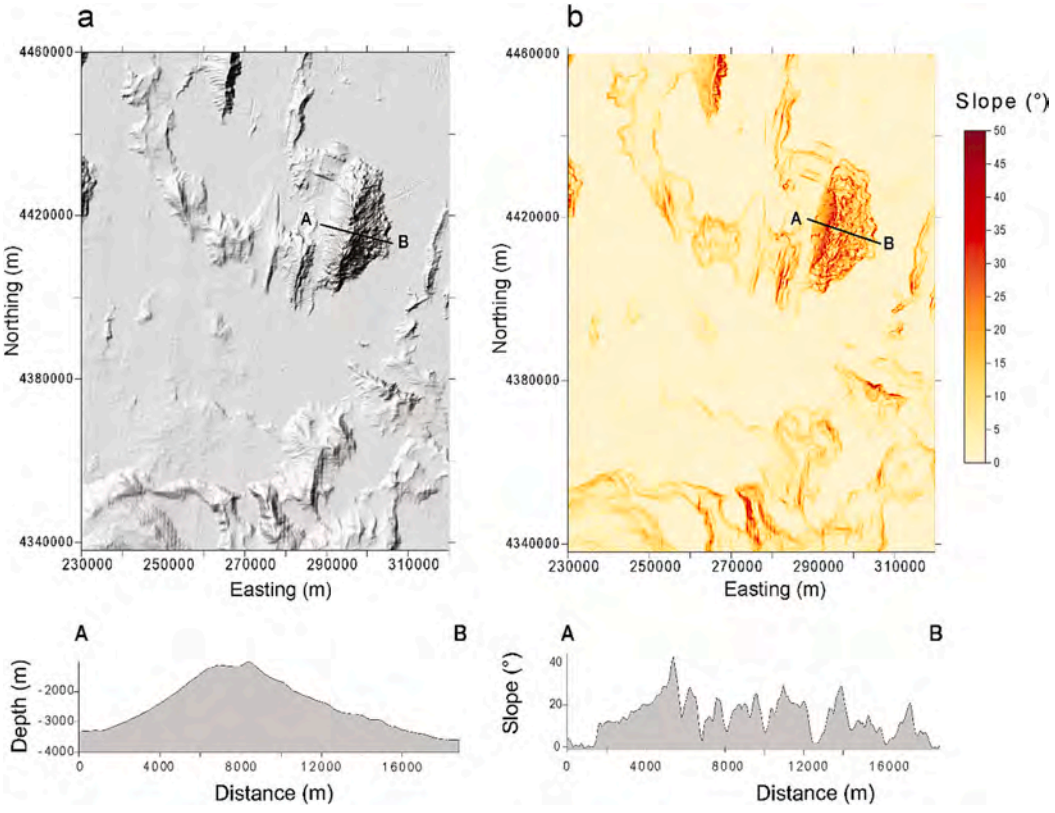

Fig. 2. (a) Bathymetric and (b) slope maps of the Vavilov Basin and Vavilov Seamount. The cross sections A-B in the maps report the variation in depth (left) and slope (right) across the Vavilov Seamount.

m of the Vavilov seamount and neighbouring areas. High resolution bathymetry of the seamount has been integrated with a 200 m grid cell EMODNET dataset (EMODnet digital bathymetry (DTM), 2023) obtaining a regional overview of the VB seafloor morphology. The data are projected in the WGS84 UTM Zone 33 N coordinate system.

3.2. Morphometric analysis and criteria for the detection of landslides

A morphometric analysis of the Vavilov DEM has been carried out by calculating the slope and aspect maps (both in degrees), and the range map with the software Surfer 13.0.383 by Golden Software. The range measures the maximum difference in altitude within a 5 × 5 cell area. The SagaGIS software (Conrad et al., 2015), version 8.0.1, has been used to produce the maps of the convergence index (Claps et al., 1996), which ranges from −100 (valleys) to +100 (ridges) with 0 representing flat areas, and geomorphons (Jasiewicz and Stepinski, 2013), which includes the classes flat, peak or summit, ridge, shoulder, spur, slope, hollow, footslope, valley, and pit or depression. To identify past slides at VV, we use the bathymetry, slope, and aspect maps (Fig. 3) to identify amphitheatre-shaped scars located at the top of elongated morphological depressions characterized by a convex-upward bathymetry. Following Masson et al. (2006), Hungr et al. (2014), and Zhu et al. (2015), these are the main geomorphological criteria to recognize submarine and subaerial slides when other data, e.g., deposits detected from seismic lines, are unavailable. We do not use stability analysis methods to determine the stability of the VV flanks because information on the physical properties of the rocks, the rock type, and the attitude of lava flows and pyroclastics are unknown.

3.3. Numerical codes for landslide and tsunami simulations

The landslide-tsunami scenarios are reproduced by means of a set of numerical models developed by the tsunami research team of the Bologna University and already applied to several published scenarios and historical cases (e.g., Zaniboni et al., 2013; Zaniboni et al., 2014; Gallotti et al., 2020; Gallotti et al., 2021; Zaniboni et al., 2021). Firstly, the model UBO-BLOCK2 divides the sliding mass into a series of blocks passible of deformation but not of changing volume during the motion. The model computes the surface-adherent slide motion considering gravity, buoyancy, water drag, and basal friction, adopting a Lagrangian approach. The blocks' interaction is governed by a distance-based law in which the deforming ability of each block is governed by a set of

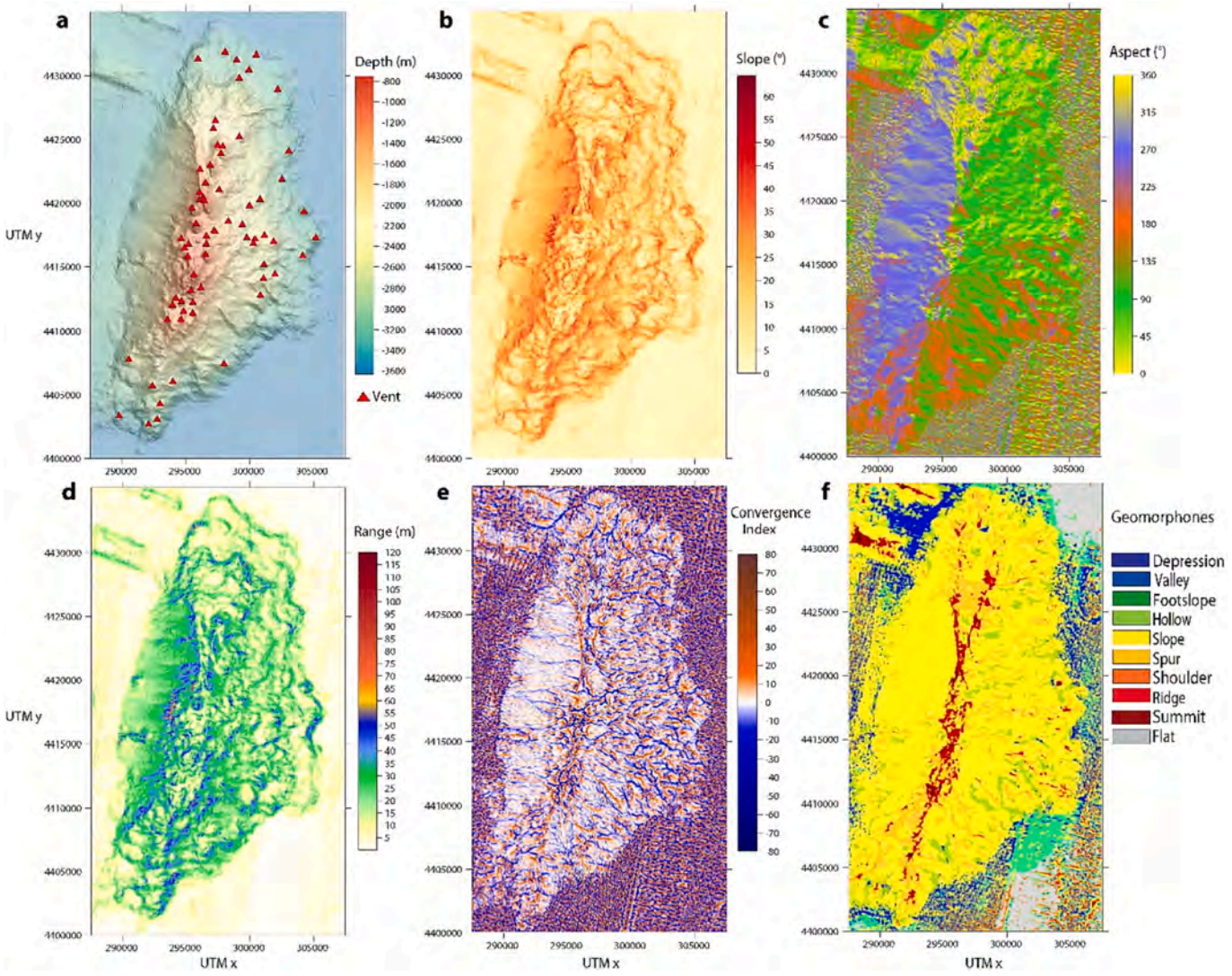

Fig. 3. (a) Bathymetry, (b) slope, (c) aspect, (d) range, (e) convergence index, and (f) geomorphons of the Vavilov Seamount obtained from the morphometric analysis of a 25 m × 25 m DSM. The red triangles in (a) are the cone-like morphologies representing possible vents. Some cones are characterized by a summit crater. The parameters of the morphometric maps (a)-(f) are defined in the text. (For interpretation of the references to colour in this figure legend, the reader is referred to the web version of this article.)

coefficients (for a detailed description of the model, see Tinti et al., 1997). The latter ones, alongside the basal friction and the water drag coefficients, are chosen following similar scenarios in submarine environments (Gallotti et al., 2020). The code UBO-TSUIMP2 calculates the time-dependent impulses the slide motion transfers to the column of water, with proper filtering techniques to manage the wavelengths smaller than the local sea depth. Eventually, the code UBO-TSUFD (Tinti and Tonini, 2013) computes the propagation of the waves inside the basin. The code implements the Navier-Stokes set of equations in the shallow water approximation. The equations are solved through a Leap-Frog numerical scheme on staggered grids. Herein, the simulations consider neither non-linear effects nor wave dispersion. As the waves propagates in the basin, a 0.2 Manning friction coefficient is considered. This value has been adopted in other studies (e.g., Sraj et al., 2014) to consider the effect of debris in the inundation process and/or to reduce the influence of high frequencies noise amplification in the coastal areas.

The tsunami generation and propagation stages are calculated on distinct grids. The generation and the initial propagation are computed on a 150 m regularly spaced grid, obtained from a 25 m spaced finer grid. The far-field propagation is calculated over a 750 m regularly spaced grid covering the whole Tyrrhenian basin. The latter is obtained from a 150 m spaced grid based on the EMODnet dataset. This gridding method is an efficient tool to avoid an excessive computational effort for the propagation stage, where the wave characteristics do not require a detailed resolution.

4. Results

4.1. Geomorphology of the Vavilov volcano

The VV occupies the central sector of the VB, which is characterized by a flat surface with a mean depth of 3600 m interrupted by two main morphological heights (Figs. 1, 2). The northern morphological height departs westward from the northern tip of the VV and consists of two parallel rectilinear ridges striking N100°E. These two ridges connect, to the west, to a third, N10°E striking, 35 km long ridge. The southern morphological high departs westward from the southern tip of the VV and consists of partly overlapping N10°E, up to 18 km long, elongated ridges. In a plane view, the southern morphological height shows an arcuate shape. The VV is a N10°E elongated, 31 km long and 14 wide volcanic complex. Its top is at 780 m b.s.l. and its height above the VB seafloor is 2820 m. The VV is characterized by an apical N10°E elongated ridge dividing the volcano in two main sectors (flanks) (Fig. 3). The east dipping (average aspect of N10°E) flank is up to 9 km wide and shows slopes between 5° and 28°, whereas the up to 5 km wide, N80°W dipping western flank has slope values between 15° and 42°. In the eastern flank, the slope decreases from the summit ridge downward, whereas no continuous slope variations have been observed in the western flank (Fig. 3a, b). In addition, while the western flank shows a relatively smooth surface with few, sub-parallel rectilinear valleys striking N100°E, the eastern flank is characterized by a rough morphology with cones, ridges, scars, valleys and near the base, hummocky surfaces (Fig. 3b, d). N10°E aligned cones with craters concentrate along the VV summit ridge, while sparse cones without a well-defined alignment occur on the eastern flank (Fig. 3a). The analysis of geomorphons as well as the maps of other morphological parameters (slope, convergence index, aspect; Fig. 3b, e, f) shows that the VV summit ridge is a relatively complex structure. Toward the north, two main diverging ridges depart from the summit central VV ridge. These delimit a morphological wedge (spur) constituting the northern flank of the VV. To the south, a similar configuration may be recognized although less evident. The VV summit ridge is almost rectilinear for most of the length of the seamount but, in its north-western sector, it curves and connects without significant breaks to the N100°E elongated ridges located in the VB bathyal plain.

4.2. Morphological evidence of landslides

Based on the morphological thematic maps reported in Fig. 3, and, in particular, on the bathymetry, slope, and aspect maps (Fig. 3a-c), we recognize four main zones depicting morphological evidence of past or potential landslides (Fig. 4). These zones are characterized by an upslope arcuate, steep scar and by downslope, convex-upward elongated depressions (Fig. 4). Slide A (A in Fig. 4 and inset) is located in the southern sector of VV and includes a south facing scar with a slope up to 40° and an about 2000 m long elongated depression developing from the base of the scar to the morphological base of VV. Slide B (B in Fig. 4 and inset) is located in the south-eastern sector of VV and it is defined by a 42°, west dipping, summit scar from which two main arcuate morphological ridges depart westward. The depressed, convex upward surface between the two ridges has a length of about 6 km. Slide C (C in Fig. 4 and inset) is located at the northern tip of VV. This slide is defined by a 35° dipping, arcuate scar and by a downslope N-S elongated depression at the mouth of which a fan-like morphology occurs. This latter morphological feature may reflect slide material although more data need to be collected to better constrain this hypothesis. Slide (D in Fig. 4 and inset) affects the eastern flank of VV. Slide D is characterized by a 32° dipping, arcuate scar along which eruptive vents occur. The downslope depressed surface is characterized by a hummocky-like morphology. As a preliminary hypothesis, we suggest that this surface may represent slide material.

Morphological evidence, e.g., hummocky surfaces in the western bathyal plain, of past flank collapses affecting the whole VV western flank are lacking. The asymmetric morphology of the seamount could be due to an asymmetric growth due to a preferential concentration of the volcanism along a summit N10°E fissure and in the eastern flank (see Fig. 2). However, the increase of the slope values from the western bathyal plain to the summit ridge is difficult to explain with a simple asymmetric growth. We do not have morphological evidence of past flank or sector collapses of the whole VV western flank, e.g., well developed amphitheatre-shaped scarps associated to carved flanks, but we cannot a priori exclude that this sector of the volcano was affected by some seafloor sliding. We will take into account this hypothesis in the simulation of a potential, past tsunami event.

4.3. Potential tsunamigenic events

For each of the four detachment areas depicted in Fig. 4, two mean slide thicknesses have been selected (20 m and 100 m). These values represent two possible, although arbitrary due to the lack of detailed data, extremes to be investigated. They are partially assumed based on the profiles in Fig. 4, which give some indication of the maximum potential removed thickness. The virtual volume of removed material in the identified landslides A, B, C, and D vary between about 0.32 km^3 and 1.7 km^3 (see Table 1). The maximum value (100 m) we adopted for the slide thickness is that of the fan-like deposit located at the base of the slide C in Fig. 4, which represents the only preserved deposit reasonably ascribable to mobilized material. All the landslide morphologies we select are two common features, i.e., a steep, upslope scar and a downslope, convex-upward, elongated depression.

Simulations' parameters (basal friction, drag coefficients, etc.) are chosen following the work by Gallotti et al. (2021) on the Marsili volcano, in virtue of the similar geological framework. Landslides on volcanic environments cover a wide range of movements, requiring distinct modelling efforts (see Schaefer et al., 2019 for a recent review). We simulate planar rock slides in which the rheology is managed by an interaction coefficient. This is based on the deformation induced by the reciprocal block interaction (see Tinti et al., 1997 for details). The classical rigid slide model approach (both planar and rotational) can represent a limit for the reconstruction of landslide induced tsunamis. Yavari-Ramshe and Ataie-Ashtiani (2017) prove that rigid slide modelling tends to overestimate the features of induced waves, not considering

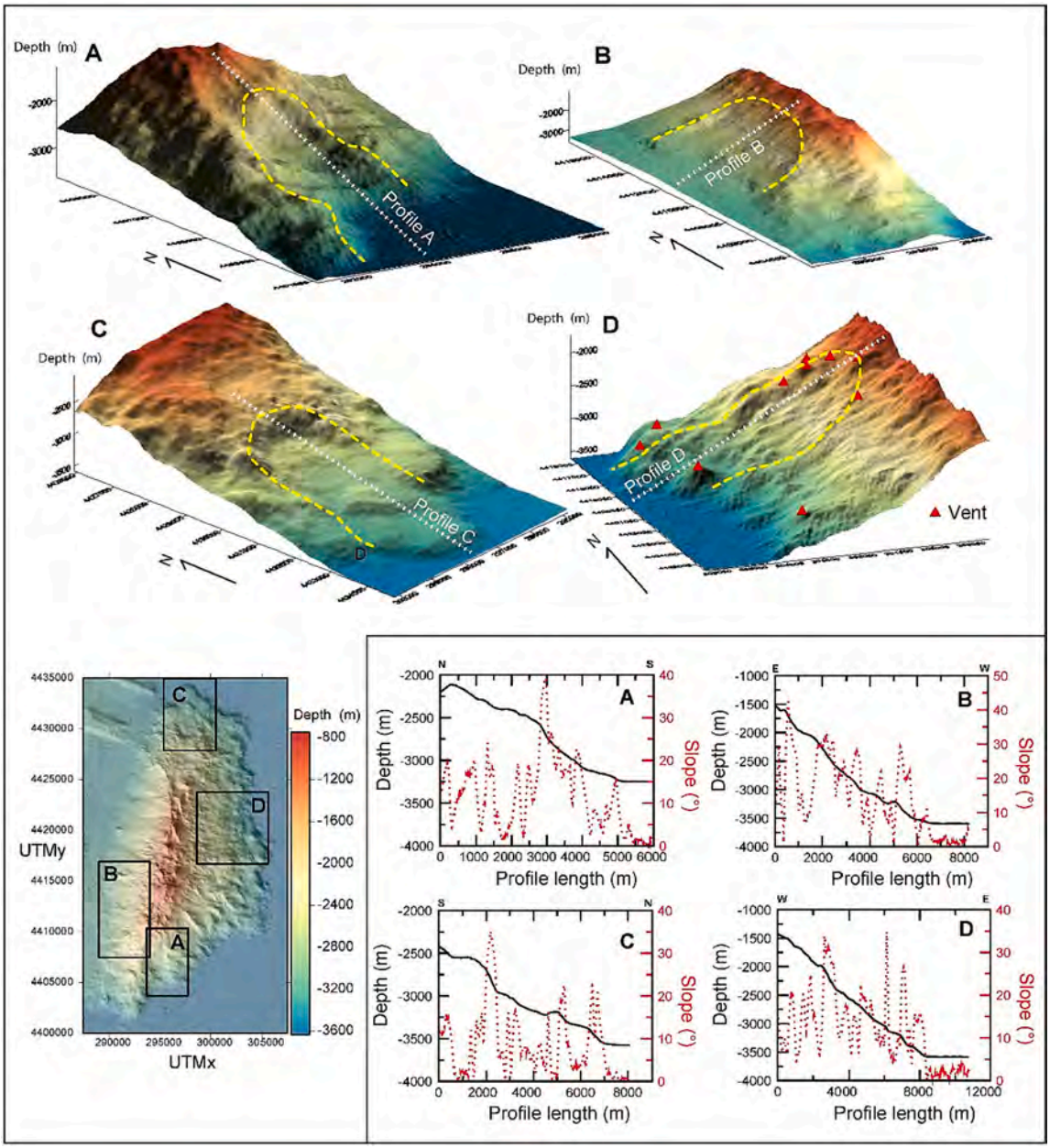

Fig. 4. Location and 3D view of the selected landslides A, B, C, and D. The yellow dashed line delimits the landslide area, and the white dashed lines define the traces of the bathymetric and slope profiles reported in the inset at lower right. (For interpretation of the references to colour in this figure legend, the reader is referred to the web version of this article.)

Table 1
Volumes and maximum slide velocities for the selected scenarios.

Scenario	Volume (km^3)	Maximum Slide Velocity (m/s)
A1	0.32	51
A2	1.28	52
B1	0.36	51
B2	1.66	52
C1	0.35	34
C2	1.50	39
D1	0.39	38
D2	1.70	37

the landslide deformations on water surface fluctuations. Nevertheless, the UBOBLOCK models are able to simulate also the block deformation during the motion with the aim of investigating the slide tsunamigenic potential, which is mostly determined in the acceleration phase of the motion (see Conway et al., 2012 for details on the main landslide features influencing the tsunami generation). This is mainly influenced by the landslide geometry and the surface steepness. Rotational slides could imply lower acceleration and thus less tsunamigenic potential. In Table 1, a recap of the slides' characteristics is shown. The slides' thickness is not the prevailing factor influencing landslide dynamics, while it plays a significant role in the tsunami generation process. We focus our attention on the water elevations above the sliding areas for the thicker slides (Fig. 5). These values represent a reference for the generated tsunamis and allow the understanding of the potentially more hazardous waves.

The highest values are found in the B2 case (Fig. 6), whose volume is 1.66 km^3. For this reason, the wave elevations along the coasts are shown only for this case. The wave heights are computed on the 10 m bathymetric line, not considering phenomena related to the local

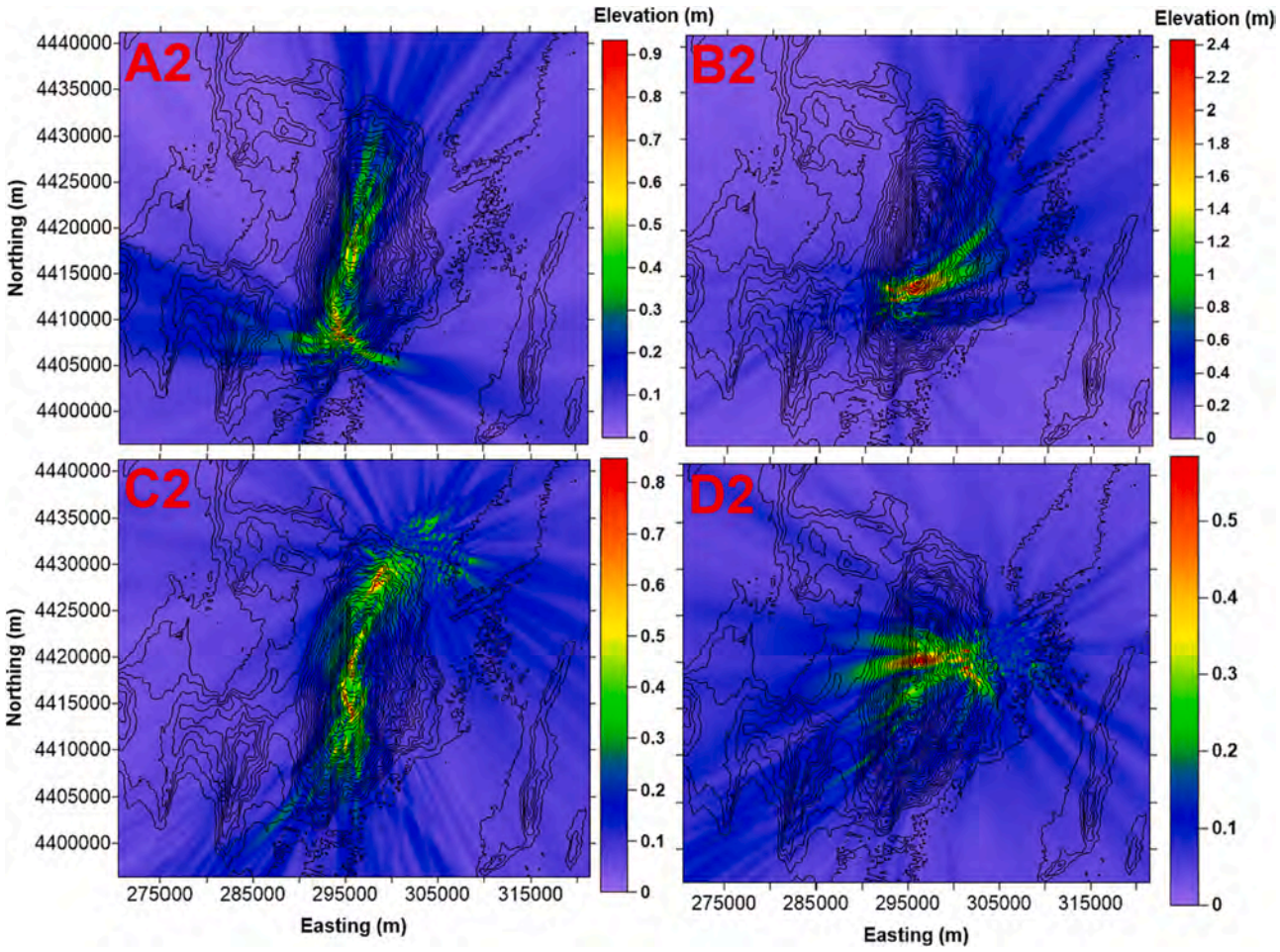

Fig. 5. Maximum water elevations computed over a time interval of 400 s on the smaller grid for the A2-D2 scenarios, i.e., the ones related to the most voluminous slides. Note that different scales for the water elevation are used in the four graphs.

shallower bathymetry. In the numerical simulations all the grid nodes with depth shallower than 10 m have been levelled to the same depth of 10 m and the coastline is treated as a vertical, perfectly reflecting wall. This choice is dictated by the fact that the estimation of the actual wave inundating the coasts requires a much finer topo-bathymetric dataset and large computational efforts that are not requested at this stage of the study. Through this kind of graphs our purpose is to elucidate the stretches of the coast potentially affected by the more dangerous waves.

4.4. *The west flank collapse: a debated event*

The west flank of the VV shows a peculiar scar-like morphology with average gradients in the order of 25°. Conversely, the east flank shows gentler slopes (see Fig. 2 and Fig. 7). The origin of this asymmetry has not been unveiled and different theories have been proposed. While some studies have suggested that the scar is the result of a past sector collapse (Caratori Tontini et al., 2010), evidence of deposits testifying single or multiple collapses as, for example, hummocky surfaces, are lacking. For the sake of completeness, in this section, we investigate the consequences of a past potential sector collapse with the aim of detecting the stretches of coasts potentially hit by the waves. The sliding mass initial thickness has been hypothesized as the result of the different gradients between the two flanks (see Fig. 7). The total volume is in the range of 19 km^3, with a mean slide thickness of 220 m.

For the sake of coherence, the model main parameters are set identical to those used for the potential events scenarios. The computed tsunami waves (Fig. 8) show maximum elevations in the range of 6–10 m on numerous peri-Tyrrhenian coasts. Pointedly, the higher values are found in the western Sardinian coasts (9 m) and in the southern part of the Campania region coasts (10 m), that are respectively to the west and to the east of the source region.

5. Discussion and conclusions

In this study, we have presented new insights about the Vavilov submarine volcano. Our new data on the location of the eruptive vents (Fig. 3a) suggest that the volcano grew asymmetrically. Most of the cones are distributed along the summit, N10°E elongated ridge and without a preferential alignment on the western flank. Therefore, the N10°E aligned cones of the ridge represent the surface expression of an eruptive fissure, i.e., a dike. The analysis of the morphometric parameters derived from the bathymetry data and, in particular, the slope and aspect maps reported in Fig. 3, allow us to identify four past landslides (Fig. 4). The morphology of such slides is characterized by an arcuate, upslope scar and downslope elongated depressions. Deposits with a maximum thickness of about 100 m characterize the slide D (Fig. 4) which is characterized by volcanic vents located along its scar. We suggest that the magma erupted along these vents upraised within the shallowest portion of the volcano by intruding a pre-existing weakness zone related to gravity instability phenomena. The landslides identified in this study do not exclude that other sectors of VV may be affected by smaller gravity instability phenomena; however, our data do not provide clear, unquestionable evidence of other potential landslides.

The VV steep slopes of the western apical zone of the N10°E summit ridge may also have acted as scars and favoured potential mass movements in the past. Although the few available data do not permit a

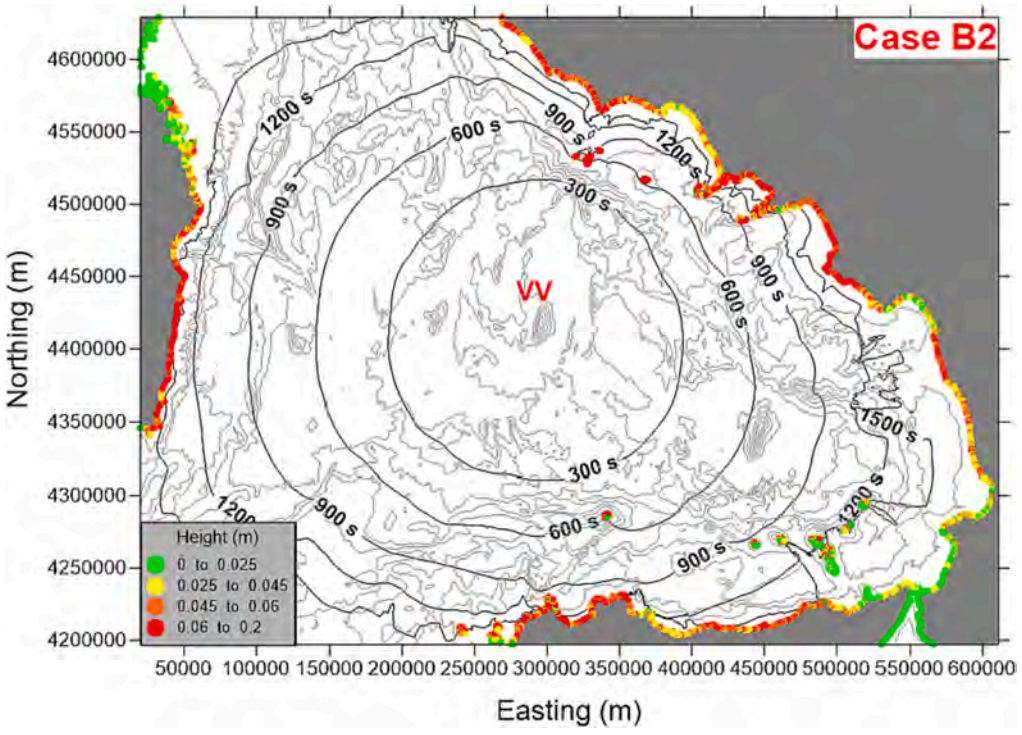

Fig. 6. Maximum water elevations along the coasts of the larger, 750-m resolution, grid for the B2 scenario within a time interval of 120 min. The black isolines mark the tsunami travel time, that is expressed in seconds.

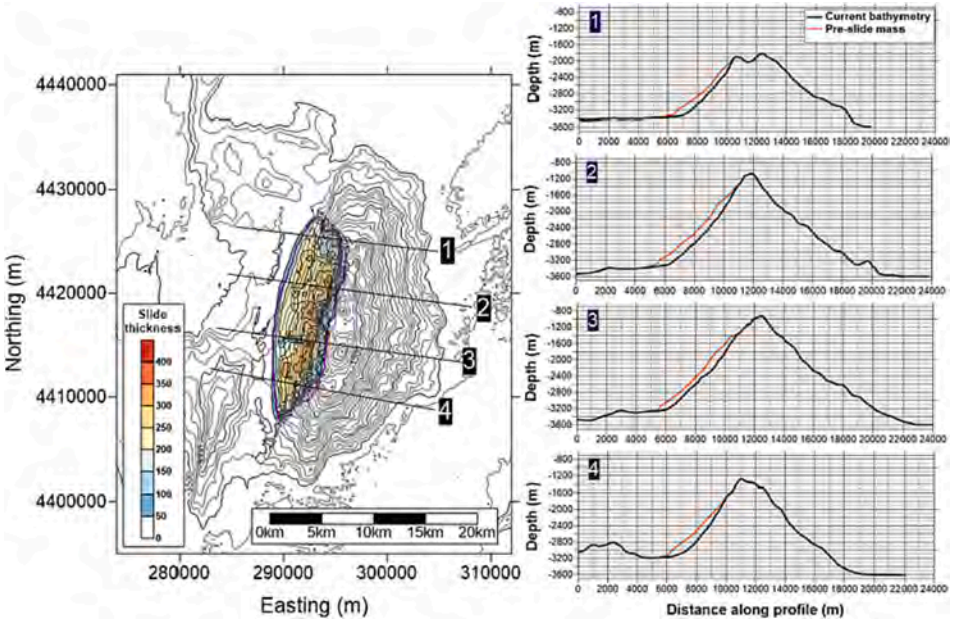

Fig. 7. Left panel: initial slide thickness for west flank collapse. Right panel: selected profiles (1–4) with the pre-slide mass represented by the orange profile.

detailed stability analysis of the identified zones (A-D, in Fig. 3b), nevertheless, seismic or volcanic activity cannot be ruled out and an investigation of the tsunamigenic potential of mass movements is needed. This is also supported by other studies of this nature in the Tyrrhenian basin (Gallotti et al., 2020; Gallotti et al., 2021). For each zone, two slides of distinct medium thickness have been simulated. Slide volumes range between 0.32 km^3 and 3.6 km^3. Results prove that the sliding volume does not influence the general dynamics: maximum velocity values are comparable in each zone (Table 1). The slide reaches higher velocities in the A and B cases (51–56 km/h), presenting a less deep detachment area (−1600 m at the headscarp). C and D slides detach some 600 m and 800 m below, respectively, and in a less steep section of the volcano. For this reason, velocity maxima are in the order of 34–39 m/s.

Maximum water elevations in the VV area are shown just for the more voluminous slide being the volume strongly correlated to the tsunamigenic potential (Harbitz et al., 2006). Values as high as 2.4 m are found for B2 case. This is not the case in the other simulations, showing values in the order of 0.5–0.9 m. Values in the order of a few centimetres are found for the 20 m-medium-thickness slides since the volumes are

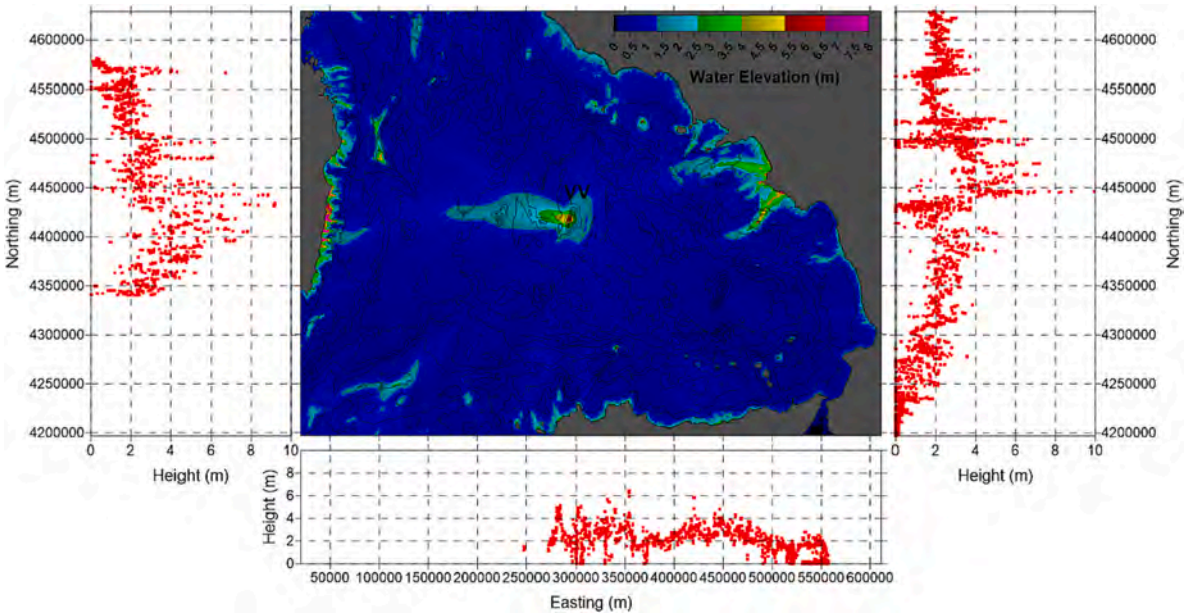

Fig. 8. Maximum water elevations in the Tyrrhenian basin for the west flank collapse (central panel). Maximum coastal elevations, computed along the 10-m isobath, are shown in red dots for different coastlines (side panels). (For interpretation of the references to colour in this figure legend, the reader is referred to the web version of this article.)

scaled by a factor of 5 with respect to the thicker ones. Water elevations along the coasts (Fig. 6 for case B2) prove that average values of 10–20 cm are found in the south-eastern Sardinia coasts, north-western Sicily coasts, and over portions of the Campania and Latium regions. The other scenarios are not shown for the sake of brevity since they involve the generation of potentially not hazardous waves (between 0.10 and few centimetres). Due to the distance to the surrounding coasts (between 120 and 300 km), the dispersion could play a role in the actual wave heights along the coasts. Thus, herein the computed values must be intended as the maximum possible. For more details on the role of wave dispersion in landslide-generated tsunamis, see Glimsdal et al. (2013). As a consequence, all the potential scenarios presented in this work could have slight implications in terms of hazards, if we exclude local effects in harbours as seen for example in the far field after the 2002 Stromboli mass failure event (Tinti et al., 2005; Maramai et al., 2005).

On the contrary, the potential prehistoric collapse of the western flank implies the generation of considerable waves in the peri-Tyrrhenian coasts (maximum values of 6–10 m). Nevertheless, the reliability of this event is still debated, and no specific studies can be found in the literature about this aspect. Indeed, this slide scenario must be considered merely as one of the possible collapses that took place on the west flank of the volcano. If the sector collapse theory will be confirmed in future studies, it could be the result of multiples collapses, also in distinct times. Eventually, signs of a tsunami of this magnitude could be found in specific stretches of coasts, but the science of tsunami deposits research is relatively young (see Costa and Andrade, 2020 for a recent review). For this reason, this study highlights the need of collecting more data on this volcano, and, in general, on the other abundant structures of the Tyrrhenian Sea.

CRediT authorship contribution statement

G. Gallotti: Conceptualization, Methodology, Formal analysis, Software, Validation, Investigation, Writing – original draft, Visualization, Writing – review & editing. **F. Zaniboni:** Software, Visualization, Writing – review & editing. **D. Arcangeli:** Conceptualization, Methodology, Software, Visualization, Data curation. **C. Angeli:** Methodology, Software, Visualization. **A. Armigliato:** Methodology, Software, Visualization, Supervision, Writing – review & editing. **L. Cocchi:** Data curation, Visualization, Writing – review & editing. **F. Muccini:** Data curation, Visualization. **M. Zanetti:** Methodology, Software, Visualization. **S. Tinti:** Resources, Writing – review & editing, Supervision, Funding acquisition. **G. Ventura:** Data curation, Investigation, Visualization, Writing – original draft, Writing – review & editing, Visualization, Supervision.

Declaration of Competing Interest

The authors declare that they have no known competing financial interests or personal relationships that could have appeared to influence the work reported in this paper.

Data availability

The data that has been used is confidential.

Acknowledgements

Authors are sincerely grateful to captain, officers and crew of R/V Magnaghi of Italian Navy for their support during VAV11 expedition. The authors wish to thank Sebastian Watt and the other reviewers that are anonymous for their constructive and useful suggestions.

References

Cande, S.C., Kent, D.V., 1995. Revised calibration of the geomagnetic polarity time scale for the late cretaceous and Cenozoic. J. Geophys. Res. 100, 6093–6095.

Caratori Tontini, F., Cocchi, L., Muccini, F., Carmisciano, C., Marani, M., Bonatti, E., Ligi, M., Boschi, E., 2010. Potential-field modelling of collapse-prone submarine volcanoes in the southern Tyrrhenian Sea (Italy). Geophys. Res. Lett. 37, L03305. https://doi.org/10.1029/2009GL041.

Cella, F., Fedi, M., Florio, G., Paoletti, V., Rapolla, A., 2008. A review of the gravity and magnetic studies in the Tyrrhenian Basin and its volcanic districts. Ann. Geophys. 51, 1–23.

Claps, P., Fiorentino, M., Oliveto, G., 1996. Informational entropy of fractal river networks. J. Hydrol. 187, 145–156.

Cocchi, L., Caratori Tontini, F., Muccini, F., Marani, M.P., Bortoluzzi, G., Carmisciano, C., 2009. Chronology of the transition from a spreading ridge to an accretional seamount in the Marsili backarc basin (Tyrrhenian Sea). Terra Nova 21, 369–374. https://doi.org/10.1111/j.1365-3121.2009.00891.x.

Cocchi, L., Passaro, S., Tontini, F.C., Ventura, G., 2017. Volcanism in slab tear faults is larger than in island-arcs and back-arcs. Nat. Commun. 8, 1451. https://doi.org/10.1038/s41467-017-01626-w.

Conrad, O., Bechtel, B., Bock, M., Dietrich, H., Fischer, E., Gerlitz, L., Wehberg, J., Wichmann, V., Bohner, J., 2015. System for Automated Geoscientific analyses (SAGA) v. 2.1.4. Geosci. Model Dev. 8, 1991–2007. https://doi.org/10.5194/gmd-8-1991-2015.

Conway, Kim W., Vaughn Barrie, J., Thomson, R.E., 2012. Submarine slope failures and tsunami hazard in coastal British Columbia: Douglas Channel and Kitimat arm. Natural Resources Canada. https://doi.org/10.4095/291732.

Costa, P.J.M., Andrade, C., 2020. Tsunami deposits: present knowledge and future challenges. Sedimentology 67, 1189–1206. https://doi.org/10.1111/sed.12724.

Dao, M.H., Tkalich, P., 2007. Tsunami propagation modelling – a sensitivity study. Nat. Hazards Earth Syst. Sci. 7, 741–754. https://doi.org/10.5194/nhess-7-741-2007.

De Astis, G., Ventura, G., Vilardo, G., 2003. Geodynamic significance of the Aeolian volcanism (Southern Tyrrhenian Sea, Italy) in light of structural, seismological, and geochemical data. Tectonics 22, TC001506. https://doi.org/10.1029/2003TC001506.

Doglioni, C., 1991. A proposal of kinematic modeling for W-dipping subduction-possible application to the Tyrrhenian–Apennine system. Terra Nova 3, 423–434. https://doi.org/10.1111/j.1365-3121.1991.tb00172.x.

Doglioni, C., Harabaglia, P., Merlini, S., Mongelli, F., Peccerillo, C., Piromallo, C., 1999. Orogens and slab vs. their direction of subduction. Earth Sci. Rev. 45, 167–208. https://doi.org/10.1016/S0012-8252(98)00045-2.

Doglioni, C., Innocenti, F., Morellato, C., Procaccianti, D., Scrocca, D., 2004. On the Tyrrhenian Sea opening. Memorie Descrittive Carta Geologica d'Italia 64, 147–164.

EMODnet digital bathymetry (DTM), 2023. Brussels: The European Marine Observation and Data Network, European Maritime and Fisheries Fund. https://doi.org/10.12770/18ff0d48-b203-4a65-94a9-5fd8b0ec35f6.

Esposti Ongaro, T., Michieli Vitturi, M., Cerminara, M., Fornaciai, A., Nannipieri, L., Favalli, M., Calusi, B., Macías, J., Castro, M.J., Ortega, S., González-Vida, J.M., Escalante, C., 2021. Modelling tsunamis generated by submarine landslides at Stromboli volcano (Aeolian Islands, Italy): a numerical benchmark study. Front. Earth Sci. 9, 628652 https://doi.org/10.3389/feart.2021.628652.

Faccenna, C., Mattei, M., Funiciello, D., Jolivet, L., 1997. Styles of back-arc extension in the Central Mediterranean. Terra Nova 9, 126–130. https://doi.org/10.1046/j.1365-3121.1997.d01–12.x.

Faccenna, C., Funiciello, F., Giardini, D., Lucente, P., 2001. Episodic back-arc extension during restricted mantle convection in the Central Mediterranean. Earth Planet. Sci. Lett. 187, 105–116. https://doi.org/10.1016/S0012-821X(01)00280-1.

Faggioni, O., Pinna, E., Savelli, C., Schreider, A.A., 1995. Geomagnetism and age study of Tyrrhenian seamounts. Geophys. J. Int. 123, 915–930. https://doi.org/10.1111/j.1365-246X.1995.tb06898.x.

Fornaciai, A., Favalli, M., Nannipieri, L., 2019. Numerical simulation of the tsunamis generated by the Sciara del Fuoco landslides (Stromboli Island, Italy). Sci. Rep. 9 (18), 542. https://doi.org/10.1038/s41598-019-54,949-7.

Gallotti, G., Passaro, S., Armigliato, A., Zaniboni, F., Pagnoni, G., Wang, L., Sacchi, M., Tinti, S., Ligi, M., Ventura, G., 2020. Potential mass movements on the Palinuro volcanic chain (southern Tyrrhenian Sea, Italy) and consequent tsunami generation. J. Volcanol. Geotherm. Res. 404 (107), 025. https://doi.org/10.1016/j.jvolgeores.2020.107025.

Gallotti, G., Zaniboni, F., Pagnoni, G., Romagnoli, C., Gamberi, F., Marani, M., Tinti, S., 2021. Tsunamis from prospected mass failure on the Marsili submarine volcano flanks and hints for tsunami hazard evaluation. Bull. Volcanol. 83, 2. https://doi.org/10.1007/s00445-020-01425-0.

Glimsdal, S., Pedersen, G.K., Harbitz, C.B., Løvholt, F., 2013. Dispersion of tsunamis: does it really matter? Nat. Hazards Earth Syst. Sci. 13, 1507–1526. https://doi.org/10.5194/nhess-13-1507-2013.

Grilli, S.T., Tappin, D.R., Carey, S., Watt, S.F.L., Ward, S.N., Grilli, A.N., Engwell, S.L., Zhang, C., Kirby, J.T., Schambach, L., Muin, M., 2019. Modelling of the tsunami from the December 22, 2018 lateral collapse of Anak Krakatau volcano in the Sunda Straits, Indonesia. Sci. Rep. 9 (11), 946. https://doi.org/10.1038/s41598-019-48,327-6.

Harbitz, C., Løvholt, F., Pedersen, G., Masson, D., 2006. Mechanisms of tsunami generation by submarine landslides: A short review. Norsk Geologisk Tidsskrift. 86, 255–264.

Hungr, O., Leroueil, S., Picarelli, L., 2014. The Varnes classification of landslide types, an update. Landslides 11, 167–194. https://doi.org/10.1007/s10346-013-0436-y.

Jasiewicz, J., Stepinski, T.F., 2013. Geomorphons–a pattern recognition approach to classification and mapping of landforms. Geomorphology 182, 147–156. https://doi.org/10.1016/j.geomorph.2012.11.005.

Kastens, K.A., Mascle, J., Auroux, C., Bonatti, E., Broglia, C., Channell, J., Curzi, P., Emeis, K., Glacon, G., Hasegawa, S., Hieke, W., Mascle, G., McCoy, F., McKenzie, J., Mendelson, J., Muller, C., Rehault, J.-P., Robertson, A., Sartori, R., Sprovieri, R., Torii, M., 1988. ODP Leg 107 in the Tyrrhenian Sea: Insights into Passive Margin and Back-arc basin evolution. Geol. Soc. Amer. Bull. 100, 1140–1156. https://doi.org/10.1130/0016-7606(1988)100 < 1140:OLITTS>2.3.CO;2.

Kirby, J.T., Grilli, S.T., Horrillo, J., Liu, P.L., Nicolsky, D., Abadie, S., Ataie-Ashtiani, B., Castro, M.J., Clous, L., Escalante, L., Fine, I., González-Vida, J.M., Løvholt, F., Lynett, P., Ma, G., Macías, J., Ortega, S., Shi, F., Yavari-Ramshe, S., Zhnag, C., 2022. Validation and inter-comparison of models for landslide tsunami generation. Ocean Modelling 170 (101), 943. https://doi.org/10.1016/j.ocemod.2021.101943.

Malinverno, A., Ryan, W.B.F., 1986. Extension in the Tyrrhenian Sea and shortening in the Apennines as a result of arc migration driven by sinking of lithosphere. Tectonics 5, 227–245. https://doi.org/10.1029/TC005i002p00227.

Manu-Marfo, D., Aoudia, A., Pachhai, S., Kherchouche, R., 2019. 3D shear wave velocity model of the crust and uppermost mantle beneath the Tyrrhenian basin and margins. Sci. Rep. 9, 3609. https://doi.org/10.1038/s41598-019-40,510-z.

Maramai, A., Graziani, L., Alessio, G., Burrato, P., Colini, L., Cucci, L., Nappi, R., Nardi, A., Vilardo, G., 2005. Near- and far-field survey report of the 30 December 2002 Stromboli (Southern Italy) tsunami. Mar. Geol. 215, 93–106. https://doi.org/10.1016/j.margeo.2004.11.009.

Marani, M.P., Gamberi, F., 2004. Structural framework of the Tyrrhenian Sea unveiled by seafloor morphology. In: Marani, M.P., Gamberi, F., Bonatti, E. (Eds.), From Seafloor to Deep Mantle: Architecture of the Tyrrhenian Backarc Basin: APAT, Memorie Descrittive Carta Geologica d'Italia, 44, pp. 97–108.

Mascle, J., Rehault, J.P., 1990. A revised seismic stratigraphy of the Tyrrhenian Sea: implications for the basin evolution. In: Kastens, K.A., Mascle, J., et al. (Eds.), Proc. ODP, Sci. Results, 107: College Station TX (Ocean Drilling Program), pp. 617–636.

Masson, D.G., Harbitz, C.B., Wynn, R.B., Pedersen, G., Løvholt, F., 2006. Submarine landslides: processes, triggers and hazard prediction. Phil. Trans. R. Soc. A. 364, 2009–2039. https://doi.org/10.1098/rsta.2006.1810.

Mauffret, A., Contrucci, I., Brunet, C., 1999. Structural evolution of the Northern Tyrrhenian Sea from new seismic data. Mar. Pet. Geol. 16, 381–407. https://doi.org/10.1016/S0264-8172(99)00004-5.

Nagai, K., Muhari, A., Pakoksung, K., Watanabe, M., Suppasri, A., Arikawa, T., Imamura, F., 2021. Consideration of submarine landslide induced by 2018 Sulawesi earthquake and tsunami within Palu Bay. Coastal. Eng. J. 1, 1–21. https://doi.org/10.1080/21664250.2021.1933749.

Paris, A., Heinrich, P., Paris, R., Abadie, S., 2020. The December 22, 2018 Anak Krakatau, Indonesia, Landslide and Tsunami: Preliminary Modelling Results. Pure Appl. Geophys. 177, 571–590. https://doi.org/10.1007/s00024-019-02394-y.

Patacca, E., Sartori, R., Scandone, P., 1990. Tyrrhenian Basin and Apenninic arcs: kinematic relations since Late Tortonian times. Memorie della Società Geologica Italiana 45, 425–451.

Pensa, A., Pinton, A., Vita, L., Bonamico, A., De Benedetti, A.A., Giordano, G., 2019. Atlas of Italian Submarine Volcanic Structures. Mem. Descr. Carta Geol. d'It. 104, 77–183.

Prada, M., Ranero, C.R., Sallarès, V., Zitellini, N., Grevemeyer, I., 2016. Mantle exhumation and sequence of magmatic events in the Magnaghi-Vavilov Basin (Central Tyrrhenian, Italy): New constraints from geological and geophysical observations. Tectonophysics 689, 133–142. https://doi.org/10.1016/j.tecto.2016.01.041.

Ren, Z., Wang, Y., Wang, P., Hou, J., Gao, Y., Zhao, L., 2020. Numerical study of the triggering mechanism of the 2018 Anak Krakatau tsunami: eruption or collapsed landslide? Nat. Hazards 102, 1–13. https://doi.org/10.1007/s11069-020-03907-y.

Robin, C., Colantoni, P., Gennesseaux, M., Rehault, J.P., 1987. Vavilov seamount: A mildly alkaline Quaternary volcano in the Tyrrhenian Basin. Mar. Geol. 78 (125), 136. https://doi.org/10.1016/0025-3227(87)90071-5.

Rovere, M., Bo, M., Alessi, J., Paoli, C., Villani, N., Vassallo, P., Fiori, C., Roccatagliata, N., 2016. 3. Seamounts and Seamount-Like Structures of the Tyrrhenian Sea. In: Atlas of the Mediterranean seamounts and seamount-like structures (pp. 111–184) Publisher: IUCN, Gland, Switzerland and Málaga, Spain Editors: Maurizio Würtz, Marzia Rovere.

Royden, L., 1988. Flexural behaviour of the continental lithosphere in Italy constraints imposed by gravity and deflection data. J. Geophys. Res. 93, 7747–7766. https://doi.org/10.1029/JB093iB07p07747.

Sartori, R., Torelli, L., Zitellini, N., Carrara, G., Magaldi, M., Mussoni, P., 2004. Crustal features along a W–E Tyrrhenian transect from Sardinia to Campania margins (Central Mediterranean). Tectonophysics 383, 171–192. https://doi.org/10.1016/j.tecto.2004.02.008.

Savelli, C., 2002. Time–space distribution of magmatic activity in the western Mediterranean and peripheral orogens during the past 30 Ma (a stimulus to geodynamic considerations). J. Geodynamics 34, 99–126. https://doi.org/10.1016/S0264-3707(02)00026-1.

Savelli, C., Ligi, M., 2017. An updated reconstruction of basaltic crust emplacement in Tyrrhenian Sea. Italy. Sci. Rep. 7 (18), 024. https://doi.org/10.1038/s41598-017-17,625-2.

Savelli, C., Schrieder, A.A., 1991. The opening processes in the deep Tyrrhenian basins of Marsili and Vavilov, as deduced from magnetic and chronological evidence of their igneous crust. Tectonophysics 190, 119–131. https://doi.org/10.1016/0040-1951(91)90358-Y.

Schaefer, L.N., Di Traglia, F., Chaussard, E., Lu, Z., Nolesini, T., Casagli, N., 2019. Monitoring volcano slope instability with Synthetic Aperture Radar: A review and new data from Pacaya (Guatemala) and Stromboli (Italy) volcanoes. Earth-science reviews 192, 236–257. https://doi.org/10.1016/j.earscirev.2019.03.009.

Scrocca, D., Carminati, E., Doglioni, C., Procaccianti, D., 2012. Tyrrhenian sea. In: Robert, D.G., Bally, A.W. (Eds.), Phanerozoic Passive Margins, Cratonic Basins and Global Tectonic Maps, vol. 1C. Elsevier. https://doi.org/10.1016/B978-0-444-56,357-6.00012-3.

Sraj, I., Mandli, K.T., Knio, O.M., Dawson, C.N., Hoteit, I., 2014. Uncertainty quantification and inference of Manning's friction coefficients using DART buoy data during the Tōhoku tsunami. Ocean Modelling 83, 82–97. https://doi.org/10.1016/j.ocemod.2014.09.001.

Tinti, S., Tonini, R., 2013. The UBO-TSUFD tsunami inundation model: validation and application to a tsunami case study focused on the city of Catania, Italy. Nat. Hazards Earth Syst. Sci. 13, 1795–1816. https://doi.org/10.5194/nhess-13-1795-2013.

Tinti, S., Bortolucci, E., Vannini, C., 1997. A block-based theoretical model suited to gravitational sliding. Nat. Hazards 16, 1–28. https://doi.org/10.1023/A:1007934804464.

Tinti, S., Manucci, A., Pagnoni, G., Armigliato, A., Zaniboni, F., 2005. The 30 December 2002 landslide-induced tsunamis in Stromboli: sequence of the events reconstructed from the eyewitness accounts. Nat. Hazards Earth Syst. Sci. 5, 763–775. https://doi.org/10.5194/nhess-5-763-2005.

Tozer, B., Sandwell, D.T., Smith, W.H.F., Olson, C., Beale, J.R., Wessel, P., 2019. Global bathymetry and topography at 15 arc sec: SRTM15+. Earth and Space Science 2019, 6. https://doi.org/10.1029/2019EA00065.

Williams, R., Rowley, P., Garthwaite, M.C., 2019. Reconstructing the Anak Krakatau flank collapse that caused the December 2018 Indonesian tsunami. Geology 47, 973–976. https://doi.org/10.1130/G46517.1.

Yavari-Ramshe, S., Ataie-Ashtiani, B., 2016. Numerical modelling of subaerial and submarine landslide-generated tsunami waves—recent advances and future challenges. Landslides 13, 1325–1368. https://doi.org/10.1007/s10346-016-0734-2.

Yavari-Ramshe, S., Ataie-Ashtiani, B., 2017. A rigorous finite volume model to simulate subaerial and submarine landslide-generated waves. Landslides 14, 203–221. https://doi.org/10.1007/s10346-015-0662-6.

Zaniboni, F., Pagnoni, G., Tinti, S., Della Seta, M., Fredi, P., Marotta, E., Orsi, G., 2013. The potential failure of Monte Nuovo at Ischia Island (Southern Italy): numerical assessment of a likely induced tsunami and its effects on a densely inhabited area. Bull. Volcanol. 75, 763. https://doi.org/10.1007/s00445-013-0763-9.

Zaniboni, F., Armigliato, A., Pagnoni, G., Tinti, S., 2014. Continental margins as a source of tsunami hazard: the 1977 Gioia Tauro (Italy) landslide-tsunami investigated through numerical modelling. Mar. Geol. 357, 210–217. https://doi.org/10.1016/j.margeo.2014.08.011.

Zaniboni, F., Pagnoni, G., Paparo, M.A., Gauchery, T., Rovere, M., Argnani, A., Armigliato, A., Tinti, S., 2021. Tsunamis from submarine collapses along the Eastern Slope of the Gela Basin Strait of Sicily. Front. Earth Sci. 8 (602), 171. https://doi.org/10.3389/feart.2020.602171.

Zhu, C., Jia, Y., Liu, X., Zhang, H., Wen, M., Huang, M., Shan, H., 2015. Classification and genetic machanism of submarine landslide: a review. Mar. Geol. & Quarter. Geol. 35, 153–163. https://doi.org/10.16562/j.cnki.0256-1492.2015.06.016.